Precision limits of magnetic T^3-atomic gravimetry due to atomic cloud expansion

Edgar Zuniga and Eduardo Gomez*
Instituto de Física, Universidad Autónoma de San Luis Potosí, San Luis Potosí 78295, Mexico

Luis Octavio Castanos-Cervantes
Tecnologico de Monterrey, Escuela de Ingenieria y Ciencias, Ciudad de Mexico 14380, Mexico

(Received 14 June 2023; accepted 16 November 2023; published 4 January 2024)

A promising alternative for atomic gravimetry has been proposed using a magnetic-field gradient, which has a T^3 scaling on the phase and does not require counterpropagating Raman beams. We analyze the limits in the precision of this method coming from the thermal expansion of the atomic cloud. We determine the requirements of microwave power and magnetic-field gradient to keep a resonant excitation. We find that there is a minimum microwave power required for the measurement. At high microwave powers, the relative precision in gravimetry (σ_g/g) approaches 10^{-7} in a single measurement, which is good enough for many field applications.

DOI: 10.1103/PhysRevA.109.013304

I. INTRODUCTION

In the last decades, atom interferometry has emerged as an important tool for a wide range of applications [1,2] that include gyroscopes [3,4], gradiometers [5], and gravimeters [6] for inertial sensing and navigation [7]; gravitational-wave detection [8–10]; measurement of the fine-structure constant [11] and the gravitational constant G [12]; and tests of general relativity [13]. Furthermore, portable gravimetric sensors based on atom interferometry [14–16] have promising applications in climate research [17], geodesy [18], archaeology [19,20], determination of water content [21], and monitoring of volcano activity [22]. A comprehensive review of the field of atom interferometry can be found in Refs. [23,24], and a brief review of atom gravimetry is given in Ref. [25].

Due to its fundamental and practical importance, special attention has been put to the light-pulse atom interferometer originally proposed by Kasevich and Chu in 1991 [26,27]. Several alternatives have been proposed to improve this interferometer. Some of them try to increment the sensitivity by increasing the relative phase between the arms of the interferometer. This can be achieved by increasing the size of the momentum-space splitting. Typically, the momentum transferred by a two-photon process is $2\hbar k$ where k is the wave number. However, various techniques have been explored to achieve larger relative momentum transfer. Early studies demonstrated momentum transfers in the order of a few multiples of photon recoil momentum ($\hbar k$) [28–30]. Subsequent advancements pushed the limits, achieving transfers of tens [31–34] and more than 100 [35–37] multiples. Notably, a remarkable milestone was reached with an impressive momentum transfer of $408\hbar k$ [38].

Nevertheless, large momentum transfer is not the only way to increase the relative phase between the coherent superposition of states. Recently, atomic interferometers for which the relative phase scales up as T^3 instead of T^2 (where T is the time between pulses) have been reported. In this type of interferometer, the T^3 behavior is obtained by separating both paths with the help of a constant acceleration difference between them, instead of a relative velocity difference [39]. To the best of our knowledge, the first experimental realization of an atomic interferometer showing a T^3 scaling of the phase (that was not due to gravity gradients or configurations sensitive to rotations) was obtained by using the continuous-acceleration Bloch technique [40,41]. In this method, the difference in acceleration is achieved by performing Bloch oscillations in an optical lattice. This interferometer did not exhibit a purely cubic phase, as it also contained a quadratic phase term that was introduced by the initial momentum separation created by the use of a Bragg-diffraction pulse acting as a beam splitter. In order to observe a purely cubic phase, the relative difference in acceleration has to be caused by an external field [39,42]. As far as we know, the first implementation of this type of atomic interferometer showing a sole cubic phase was reported by Zimmermann *et al.* [43].

In field-enhanced atom interferometry, the matter waves in the two arms of the interferometer are split due to a difference in acceleration, rather than velocity, resulting from the application of an external field that acts distinctly on the two arms. The external field can either be electric or magnetic in nature [42,44]. The T^3 interferometer proposed in Ref. [43] and subsequent experiments have been carried out using an external magnetic-field gradient that interacts with the total magnetic moment of the atom to induce an acceleration [39]. Implementing such interferometers is challenging as the field gradients must be controlled with high accuracy to maintain coherence, something necessary for the wave packets to be successfully recombined at the output port [45–47]. Another distinctive feature of this method is the need for four pulses with zero net momentum transfer to close the interferometer.

In the literature, two main types of T^3 interferometers are described. One type involves keeping the magnetic-field gradient constant in time while the internal state of the atom

*egomez@ifisica.uaslp.mx

is being changed in some way [43]. The other type, named the Stern-Gerlach T^3-atomic interferometer, involves keeping the atom in the same internal state while the magnetic-field gradient is being changed through the use of magnetic pulses [48]. Although both approaches are equivalent and can measure the same cubic interferometer signal with the right choice of conditions [48], the extreme accuracy needed to control the magnetic field makes the Stern-Gerlach T^3-atomic interferometer less suitable for precision measurements. Furthermore, there exists a delay time set by the speed of the electronic circuits that limits its precision [48]. Despite these drawbacks, the Stern-Gerlach interferometer with cubic scaling of the phase has been successfully used to measure magnetic-field gradients [48]. An alternative implementation involves the use of an atom chip to generate the magnetic-field pulses [49]. By using a butterfly configuration, the T^3 interferometer becomes insensitive to constant accelerations and has been proposed as a method for measuring field gradients [50]. More recently, this type of interferometer has been suggested as a potential tool for performing interferometric experiments on macroscopic objects doped with a single spin [49,51].

We analyze the precision of a T^3 interferometer similar to the one proposed in Ref. [43]. The atom undergoes free fall in the presence of a magnetic-field gradient in the vertical direction. The interferometer takes advantage of the magnetic acceleration to physically separate a coherent superposition of hyperfine states with different sensitivities to the magnetic field. The sequence of pulses $\pi/2 \xrightarrow{T} \pi \xrightarrow{2T} \pi \xrightarrow{T} \pi/2$ closes the interferometer in position and momentum and results in the characteristic T^3 dependence of the relative phase accumulated between both states, which in this case is sensitive to the gravitational acceleration g. Unlike the T^3 interferometer proposed in Ref. [43], which uses Raman light pulses to control the internal state of the atom, we consider excitation using microwaves that eliminate the need for Raman beams, simplifying considerably the experimental setup and reducing problems related to aberrations [52], given the much bigger wavelength of the microwaves. Simpler systems are highly desirable for portable sensors given that they are robust and still reach the minimum sensitivity required for field applications.

Obtaining good precision in this kind of interferometer requires finding ways to account for the magnetic-field fluctuations, nonlinearities both in the field and in the atomic response to the field, and magnetic gradients in the transverse directions [42]. Even when this interferometer is less affected by wavefront aberrations [52] or Doppler shifts [53], there is a Zeeman shift to consider. We show that the wave-packet expansion introduces a limit on the duration of the interferometric sequence, and therefore, on the measurement precision. We identify the microwave power and magnetic-field gradient combinations that give the best sensitivity.

This paper is organized as follows. Section II gives the expression for the gravitational phase in the ideal case and establishes the spatial extent where one has resonant excitation. Section III presents the limits in the precision due to the expansion of the atomic cloud. We include two regimes, one for the case of a pure state, and the other for a trapped sample in thermal equilibrium. Here, we include all the constraints that must be fulfilled to have a properly working gravimeter, and we identify the values of microwave power and magnetic-field gradient needed to implement the experiment.

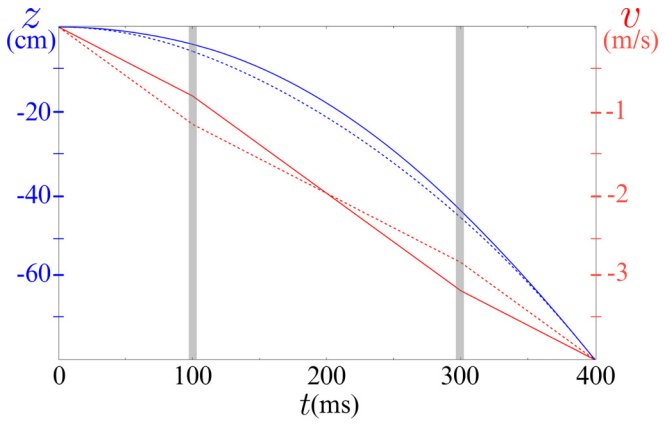

FIG. 1. Position (upper pair of curves [in blue]) and velocity (lower pair of curves [in red]) as a function of time for the upper (solid lines) and lower (dashed lines) paths. The application of the π pulses is indicated by the light gray vertical bars. We considered ^{87}Rb atoms, a gradient of $\eta = 0.05$ T/m, $T = 100$ ms, $m_F = m'_F = 1$, and $g_F = \pm 1/2$ for the two levels respectively.

II. ATOMIC GRAVIMETRY IN A MAGNETIC-FIELD GRADIENT

Atomic gravimetry is based on the splitting and recombination of an atomic wave packet. With vertical splitting, each part of the superposition evolves at a different height, giving an energy difference that is sensitive to the gravitational potential. In traditional atomic gravimetry, the two terms in the superposition have different momentum due to the momentum transfer in a Raman transition [27]. Recently, an atomic gravimeter has been proposed where the spatial separation of the wave packet happens because of a difference in acceleration [43].

Consider an atom initially in the hyperfine state $|F, m_F\rangle$. A $\pi/2$ pulse prepares a superposition between two levels $|F, m_F\rangle$ and $|F', m_{F'}\rangle$. In a magnetic-field gradient along the z axis, the two states experience a different acceleration that depends on their magnetic dipole moment, in addition to the gravitational acceleration g. After a time T, a π pulse is applied, then after $2T$ there is a second π pulse, and after an extra T a $\pi/2$ pulse closes the interferometer (Fig. 1). The scheme requires no momentum transfer so that microwaves can be used for the excitation, eliminating the need for counterpropagating Raman beams. This brings a significant simplification for atomic gravimetry, considering the complexity of the Raman beams and their sensitivity to aberrations [52].

Comparing the wave-function splitting due to a difference in position, velocity, or acceleration, the relative phase between the two paths scales with the total measurement time (T_t) as T_t, T_t^2, and T_t^3 respectively [40], or even higher for a varying acceleration. Therefore, there is an enhanced signal when using the splitting with acceleration for a long enough measurement time T_t. Here we show that there is a fundamental limitation on how long the measurement time can be due

to the wave-packet expansion, and we determine the precision that can be reached with this kind of atomic gravimeter. We limit here to an analysis of the precision of the measurement, leaving for future work the study of the systematic effects that limit the accuracy.

A. Phase of a magnetic T^3-atomic gravimeter

Consider an atom within a magnetic-field gradient in the z-axis direction subject to microwave excitation $\mathbf{B}_p(t)$. Focusing on the evolution along the z axis the Hamiltonian is [54]

$$H(t) = \frac{1}{2m}P_z^2 + mgZ + H_A - \boldsymbol{\mu}\cdot[\eta Z\hat{\mathbf{z}} + \mathbf{B}_p(t)], \quad (1)$$

with H_A the atomic structure Hamiltonian and $\boldsymbol{\mu}$ the magnetic dipole moment operator of the atom. The solution to this Hamiltonian was studied in Ref. [54], and it was used to demonstrate a velocity and position selector.

For concreteness, consider the ^{87}Rb ground states $|g_1\rangle = |F=1, m_F=1\rangle$ and $|g_2\rangle = |F'=2, m_{F'}=1\rangle$ with a coherent state spatial wave function

$$\psi(z,0) = \left(\frac{1}{2\pi\sigma_z^2}\right)^{1/4}\exp\left[-\frac{1}{4}\left(\frac{z-z_0}{\sigma_z}\right)^2 + i\frac{p_0}{\hbar}z\right], \quad (2)$$

where z_0 and p_0 are the initial position and momentum, and σ_z is the standard deviation in position or width of the atomic wave packet. Using levels with opposite magnetic responses ($g_F = 1/2$ and $g_{F'} = -1/2$) alongside the sequence of pulses described below leads to a gravimeter phase [43,48] directly proportional to g.

We suppose that the magnetic field is small so we consider only the linear Zeeman effect, which is reasonable for the relatively short measurement times that we are examining, but at high precision, one must consider the effects of the nonlinearities as well [42]. Due to the magnetic-field gradient, there is a position-dependent detuning for the transition

$$\delta(z) = \zeta(z - z_t), \quad (3)$$

where z_t is the position where the microwaves are on resonance, which we set to z_0, and

$$\zeta = (g_F m_F - g_{F'} m_{F'})\mu_B\eta/\hbar = \mu_B\eta/\hbar, \quad (4)$$

where μ_B is the Bohr magneton.

To be on resonance, the detuning $\delta(z)$ must be smaller than the Rabi frequency Ω_0 (that we assume to be real and positive). We limit the detuning to the point at which a π pulse results in no population transfer to the other state so that there is an approximately resonant excitation while $\delta(z) < \sqrt{3}\Omega_0$, or in terms of position, as long as $\Delta z = z - z_0 < \Delta z_r$, with

$$\Delta z_r = \sqrt{3}\pi\xi\frac{\Omega_0}{\zeta}, \quad (5)$$

where $0 < \xi < 1$ is a constant that we introduce to quantify how close we are to the resonant condition. We assume resonant excitation as long as $\sigma_z < \Delta z_r$ [55].

The evolution of a wave packet in a single internal level in the absence of microwaves ($\mathbf{B}_p = 0$) is given by [54]

$$\psi(z,t) = \left[\frac{1}{2\pi\sigma_z^2(t)}\right]^{1/4}\exp\left\{-\frac{1}{4}\left[\frac{z-\bar{z}(t)}{\sigma_z(t)}\right]^2 + i\Theta_p(z,t) - \frac{i}{2}\arctan\left[\frac{\hbar t}{2m\sigma_z^2(0)}\right]\right\}, \quad (6)$$

which remains a Gaussian wave packet but centered at

$$\bar{z}(t) = z_0 + v_0 t + \frac{a_\pm}{2}t^2, \quad (7)$$

where z_0 and v_0 are the initial position and velocity. The total acceleration is given by

$$a_\pm = g + (g_F m_F \mu_B \eta/m), \quad (8)$$

and depends on the value of g_F. We write it as $a_\pm$ since for the levels we are considering the magnitude of the acceleration is basically the same for both but with a sign difference (g_F changes sign). The width of the wave packet increases as

$$\sigma_z(t) = \sqrt{\sigma_z^2(0) + \left[\frac{\hbar}{2m\sigma_z(0)}\right]^2 t^2}. \quad (9)$$

Finally, Θ_p contains additional phase terms that determine the evolution of the wave packet [54]. We consider a Rabi frequency high enough that the atomic evolution during the microwave pulses has a negligible effect on the Rabi oscillations so that the wave functions associated with the external degrees of freedom remain constant and there is only a change in the internal state of the atom (see the discussion below).

By using the sequence of pulses $\pi/2 \xrightarrow{T} \pi \xrightarrow{2T} \pi \xrightarrow{T} \pi/2$, the phase difference between the two paths turns out to be given by [39,43]

$$\Delta\Phi = \frac{m}{h}(a_+^2 - a_-^2)T^3 = 2\frac{\mu_B\eta}{\hbar}gT^3, \quad (10)$$

where $T_t = 4T$ is the total measurement time. A sufficient condition to have an interferometer that is closed in position and momentum (see Fig. 1), regardless of the specific value of the total (constant) acceleration at each level, is to have the above sequence of pulses and a linear magnetic-field gradient, as can be shown by solving the equations of motion for each path [43]. As a consequence, the interferometer will also be closed in the x and y axes (with an additional transverse relative phase). The measurement of g from Eq. (10) requires the control and determination of η to the same level of precision, something that may be the most technically challenging part of this measurement.

The above result neglects the existence of phase contributions due to the quadratic Zeeman effect, gravity gradients, and nonlinear terms in the gravitational potential that cause the classical phase-space trajectories not to close. In practice, it is quite difficult to obtain a perfectly linear magnetic-field gradient, and the quadratic Zeeman effect makes things even more complicated [42], therefore clever solutions are needed to overcome these experimental challenges. Fortunately, for the measurement times considered here, the loss of visibility due to the quadratic Zeeman effect and the gravity gradients [56,57] can be neglected.

Besides the loss of visibility, the quadratic terms (in position) in the gravitational potential also introduce an additional contribution to the phase shift of Eq. (10) that causes a correction to the measured value of g [6,58]. This correction must be known with the same level of precision as that desired for the measurement and follows from considering an acceleration for the ith level that depends on the position (z) as $a_i = a_\pm + \gamma_i z$, where γ_i quantifies the quadratic correction to the potential. Then, the measured value of local gravity changes to $\tilde{g} \sim g + (\gamma_1 + \gamma_2)(z_0 + v_0 T + 3gT^2) + 2(\gamma_1 - \gamma_2)[(a_- - a_+)T^2 + (v_0^2 + gz_0 + 3gv_0 T + 9g^2 T^2)/(a_+ - a_-)] + \cdots$, where z_0 and v_0 are the initial position and initial velocity. The first term of this correction has been obtained before for light-pulse atom interferometers (see Refs. [6,58]) whereas the second term (not present in conventional light-pulse atom interferometers) is obtained following the method described in Ref. [6]. Notice that for a correction due to the gravitational gradient $\gamma_1 = \gamma_2$, whereas for a correction of magnetic origin (quadratic Zeeman effect or nonlinear magnetic-field gradient) $\gamma_1 = -\gamma_2$ (for the levels under consideration [54]). For the rest of this paper, we restrict our analysis to the case of (ideal) linear potentials.

B. Considerations to analyze the magnetic gravimeter

1. Frequency sweep of the microwaves

For the first and last $\pi/2$ pulses the centers of the wave packets for the two paths coincide, and there is an approximately resonant excitation as long as each wave packet satisfies $\sigma_z < \Delta z_r$ [Eq. (5)]. For the π pulses the two paths are spatially separated and each one has a different resonant frequency [Eq. (3)]. For a big enough separation, the frequency that excites the wave packet in one path can be set far from resonance with the other one and vice versa. Using simultaneous excitation with two microwave sources it is possible to implement the π pulse on the wave packet of each path without affecting the other one by more than a light shift. Let $\Delta d(t)$ be the separation distance between the wave-packet centers of both paths at a time t. This distance when the π pulses are applied is

$$\Delta d(T) = \Delta d(3T) = (a_+ - a_-)\frac{T^2}{2}. \tag{11}$$

We can excite the wave packet on each path with an independent frequency as long as

$$\frac{\Delta d(T)}{\Delta z_r} = \frac{\zeta}{\sqrt{3}\pi\xi\Omega_0}(a_+ - a_-)\frac{T^2}{2} \gg 1. \tag{12}$$

In traditional atomic gravimetry, there is a frequency sweep of the Raman beams that compensates for the Doppler shift of the free-falling atoms. There is no Doppler shift here since we have excitation with microwaves (although copropagating Raman transitions could be used as well) that transfer little momentum and can be set to propagate perpendicularly to the free-falling atoms with $\mathbf{B}_p(t) \perp \hat{\mathbf{z}}$. Still, it is necessary to add a frequency sweep on the microwave frequency w_m to stay in resonance with the free-falling atoms as they change their position

$$w_m(t) = w_{m_0} + \zeta(v_0 t + a_\pm t^2/2), \tag{13}$$

with w_{m_0} the initial resonant frequency. Since the acceleration $a_\pm$ is different for the two paths, there will be a different frequency change for the two microwave signals used for the π pulses.

2. Decoherence of the Rabi oscillations due to finite pulse duration

The analysis leading to Eq. (10) is based on the assumption of using pulses with a negligible duration (τ). Nevertheless, in practical scenarios, the phase shift will include an extra component arising from the evolution during the finite pulse duration. In this section, we describe how this phase contribution is characteristic of T^3 interferometry and emerges due to the distinct accelerations experienced at each level. Thus, this contribution possesses a distinct origin compared to the effect stemming from the finite pulse duration observed in conventional light-pulse atom interferometers [58].

A requirement to have full visibility of Rabi oscillations between two internal energy levels is that the spatial part of the wave function corresponding to the external degrees of freedom of both states must coincide during the pulse. However, in T^3 interferometry, this condition cannot be fulfilled because once the atom transitions from one level to another, the acceleration changes as well. To see why, consider a π pulse that is achieved by applying two consecutive $\pi/2$ pulses. The first pulse creates a superposition of the two internal energy levels but, as mentioned earlier, these two wave packets will have different accelerations. Therefore, since the frequency sweep can only be set up to follow the acceleration of one of the two wave packets, the other one will be detuned with respect to the microwaves during the application of the second $\pi/2$ pulse. What is more, the center of both wave packets will end at different positions and with different mean velocities at the end of the second pulse due to the distinct accelerations experienced by them. The effect is a reduction in the coherence of the Rabi oscillations.

In order to quantify the phase shift due to this fundamental problem, consider the phase difference between an atomic wave packet evolving within the pulse duration in the lower level (subject to acceleration a_-) and another identical wave packet undergoing evolution in the upper level (with acceleration a_+). Assuming that the centers of mass of both wave packets initially share identical position and velocity, then at the end of the pulse, each wave packet will end up with a different position and velocity. Now, consider the interference of these wave packets, specifically, the phase shift due to a difference in the final position and momentum of the wave packets on each path ($i = 1, 2$). This phase shift due to a mismatch between the classical trajectories in position and momentum space is well known [2,24,41,53,59] and is given by $\Delta\Phi_{\text{sep}}(\tau) = k_2(\tau)z_2(\tau) - k_1(\tau)z_1(\tau)$, where $z_i(\tau)$ and $\hbar k_i(\tau) = m v_i(\tau)$ can be regarded as the average position and momentum at the end of the pulse of the atomic trajectories within the cloud. Therefore, the phase difference due to the evolution during a $\pi/2$ pulse of duration $\tau = \pi/2\Omega_0$ is given by

$$\Delta\Phi_{\text{sep}}(\tau) = \frac{m}{2\hbar}[3v_{\text{rms}}(a_+ - a_-)\tau^2 + (a_+^2 - a_-^2)\tau^3], \tag{14}$$

where we have considered a common initial position $z_i(0) = 0$, and a typical velocity deviation given by $v_{\text{rms}} = \sqrt{k_B T_0/m}$

[60], and determined by the atomic cloud temperature T_0. The velocity deviation is relevant since the frequency sweep follows the center of mass of the wave packet.

Observe that this phase difference disappears when we have equal accelerations ($a_+ - a_- = 0$). The visibility of the Rabi oscillations is reduced considerably if this phase shift is larger than π by the end of the pulse, so the condition for a short pulse is

$$|\Delta\Phi_{\rm sep}(\tau)| < \pi. \tag{15}$$

A more formal treatment and a numerical calculation of the excitation with different accelerations show that Eq. (15) is indeed a good indicator for the onset of decoherence during the pulse. Later, we will show that other limitations become more important than Eq. (15) for the experimental realization and gravimetric precision. Moreover, this requirement is satisfied by the pulse duration conditions explored later on in our analysis [Eqs. (20) and (34)].

III. PRECISION OF THE MAGNETIC T^3-ATOMIC GRAVIMETER

In many field applications, a precision of several μGal is sufficient [15,17], especially if that means a simpler and more robust sensor. The precision of the magnetic atomic gravimeter relies on long fall times. For an available microwave power (P) and magnetic-field gradient (η), there is a limitation on the measurement time due to the expansion of the wave packets. To keep a resonant excitation the wave packets must remain in a region smaller than Δz_r [Eq. (5)] throughout the whole sequence. We analyze the limits on the precision set by this requirement for two different regimes. The first one (Sec. III A) considers the case of a pure state corresponding to an initial wave function on free fall starting from rest at a particular position. It describes the ultimate limitation in precision due to the expansion. Section III B analyzes the limits once the thermal distribution is taken into account and therefore gives the expected limitations on the precision in a more realistic experimental setup.

A. Expansion from a pure state

We consider first the case where the initial width of the wave function describing the external state of the atom corresponds to a pure state minimum uncertainty Gaussian wave packet. This could be achieved approximately, for example, by applying a tight selection pulse in position space [54]. The expansion of the wave packet is given by the free wave-packet expansion of Eq. (9) and its width must remain smaller than Δz_r at all times during the interferometric sequence. A big initial wave packet does not fulfill the condition, but also one that is too small expands too quickly. An initial width of $\sigma_z(0) = \Delta z_r/\sqrt{2}$ gives the longest expansion time that is equal to

$$t_1 = \frac{m}{\hbar}\Delta z_r^2 = 4T. \tag{16}$$

The relation between power and the Rabi frequency is

$$\Omega_0 = \frac{\langle e|\mu_z|g\rangle}{\hbar}\sqrt{\frac{2\mu_0 P}{cA}}, \tag{17}$$

with μ_0 the vacuum magnetic permeability, c the speed of light, A the beam area, and μ_z the magnetic moment along the polarization of the microwaves. Looking at the expression for Δz_r [Eq. (5)], the measurement time t_1 [Eq. (16)] is proportional to P/η^2. Taking a power of $P = 1$ W, a magnetic-field gradient of $\eta = 0.05$ Tm^{-1}, an area of $A = 100$ cm^2, and $\xi = 0.05$ gives $t_1 = 25$ ms. With higher power, it becomes possible to achieve measurement times comparable with other portable devices [14].

The precision in the measurement of g is given by

$$\frac{\sigma_g}{g} = \frac{\sigma_{\Delta\Phi}}{\Delta\Phi} = \frac{\sigma_{\Delta\Phi}\zeta^5}{b_1 g\xi^6}\left(\frac{A}{P}\right)^3, \tag{18}$$

where $\sigma_{\Delta\Phi}$ is the uncertainty in the phase measurement that depends on the experimental signal-to-noise ratio, $\Delta\Phi$ is given by Eq. (10), and

$$b_1 = \frac{27\pi^6}{\hbar^9}\left(\frac{m\mu_0}{c}\right)^3\langle e|\mu_z|g\rangle^6. \tag{19}$$

The precision improves with the cube of the microwave power because that extends the measurement time [Eq. (16)], and the gravimeter phase [Eq. (10)] scales with the cube of that time. Contrary to intuition, there is a decrease in precision with the gradient η (note that $\zeta \propto \eta$). This can be understood by noticing that the phase [$\Delta\Phi$, Eq. (10)] depends linearly with the gradient but also grows as T^3. The available measurement time T grows as η^{-2} [Eqs. (16) and (5)], giving the scaling on precision as η^5 [Eq. (18)].

In these interferometers, it is desirable to have a pulse duration much smaller than the time between pulses. For a $\pi/2$ pulse of duration $\tau = \pi/2\Omega_0$ this means $\tau \ll t_1/4$ or, in terms of the minimum microwave power required,

$$P \gg \frac{c}{2\mu_0}\left(\frac{1}{\langle e|\mu_z|g\rangle}\right)^2\left(\frac{2\hbar^4}{3\pi m}\right)^{2/3}A\left(\frac{\zeta}{\xi}\right)^{4/3}. \tag{20}$$

Also, the decoherence introduced by the pulses has a negligible effect when they have a duration smaller than the maximum determined by the condition of Eq. (15). Considering only the term proportional to $v_{\rm rms}$ in Eq. (14), we write the condition of Eq. (15) as a condition for the power:

$$P > \frac{3\pi\hbar^2 c}{16\mu_0\langle e|\mu_z|g\rangle^2}A\zeta v_{\rm rms}. \tag{21}$$

The free-fall time may be limited also by the size of the apparatus because there is a maximum distance $z_{\rm max}$ for the atoms in free fall. Starting from rest, the maximum measurement time, in this case, is $t_z = \sqrt{2z_{\rm max}/g}$, and equating this time to t_1 [Eq. (16)], we can relate it to the power and gradient corresponding to that precision:

$$P \leqslant \frac{c\hbar^3}{6\pi^2 m\mu_0\langle e|\mu_z|g\rangle^2}A\left(\frac{\zeta}{\xi}\right)^2\sqrt{\frac{2z_{\rm max}}{g}}, \tag{22}$$

where we have considered the average of the total acceleration $(a_+ + a_-)/2 = g$ [Eq. (8)], as the acceleration during free fall. Instead of being a requirement about minimum power like the previous two, this constraint limits the maximum precision that can be reached in the measurement. Going beyond this microwave power limit would not improve the precision, as

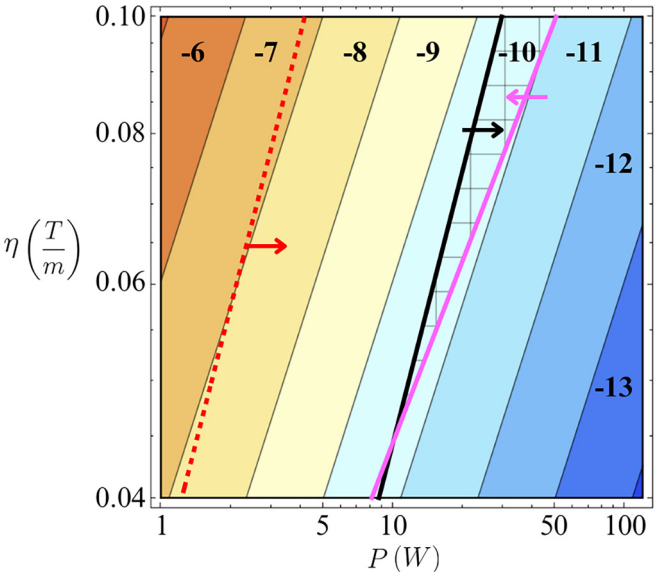

FIG. 2. Projected fractional precision of the measurement of g as a function of the microwave power (P) and magnetic-field gradient (η) for a pure Gaussian wave packet. The color code corresponds to the number of significant digits attainable in a single measurement, determined by the computation of $\log_{10}(\sigma_g/g)$ using Eq. (18). We use $A = 100$ cm^2, $\sigma_{\Delta\Phi} = 0.003$, $\xi = 0.05$, and $z_{\max} = 50$ cm. We show the boundaries set by Eq. (20) (black solid line), Eq. (22) (light pink solid line [first solid line from right to left]), and Eq. (23) (red dashed line). The limits set by Eq. (21) do not add any additional restrictions in the parameter range shown. The region that fulfills all the conditions is indicated by the mesh pattern.

the achievable time would then be limited by the chamber size, something that would be a desirable goal to reach.

The condition for addressing the wave packets of the two paths during the π pulses with independent microwave sources [Eq. (12)] gives another constraint on the power. A high power gives a bigger resonant region Δz_r [Eq. (5)], so one may intuitively think that one needs to reduce the power to achieve an excitation with independent microwave sources for the two paths during the π pulses. But the separation between the two paths $\Delta d(T)$ [Eq. (11)] increases with the measuring time $T = t_1/4$ which grows with the power [Eq. (16)]. Since this last one grows faster, higher powers are favored. The condition for excitation with independent microwave sources given by Eq. (12) gives the following condition for the power:

$$P \gg \frac{c}{\pi^2 \mu_0 \langle e|\mu_z|g\rangle^2}\left(\frac{8\sqrt{6}\hbar^4}{9m}\right)^{2/3} A\left(\frac{\zeta}{\xi^{3/2}}\right)^{4/3}, \tag{23}$$

where we have used $a_+ - a_- = \hbar\zeta/m$.

The power and the magnetic field used in the experiment determine the precision to be obtained [Eq. (18)], but their values must lie within the bounds set by the above inequalities [Eqs. (20)–(23)]. Figure 2 shows the precision that can be obtained in a single measurement as a function of the microwave power and magnetic-field gradient, as well as the regions excluded by the above conditions.

B. Expansion from an atomic sample trapped in thermal equilibrium

Now, we analyze the case of an atomic cloud at a temperature T_0 confined to a small region, as would be the case for an optical dipole trap with spatial frequency ω. The atoms are no longer in a pure state and we describe them by their density matrix (Appendix A):

$$\rho(z, z'|\beta) = \sqrt{\frac{m\omega}{2\pi\hbar\,\sinh(2\theta)}}\exp\left\{-\frac{m\omega}{2\hbar}\coth(2\theta) \times [z^2 - 2z'z\,\mathrm{sech}(2\theta) + z'^2]\right\}, \tag{24}$$

where $\theta = \hbar\omega\beta/2$ and $\beta = 1/k_B T_0$. For $\theta \ll 1$ we have near-classical behavior, whereas $\theta \gtrsim 1$ indicates the quantum regime [60,61]. We take the case of a thermal gas that is in the near-classical regime.

Starting from the ensemble described by Eq. (24), we turn the trap off and let the atoms exist in free fall with an acceleration a to obtain (Appendix B)

$$\begin{aligned}\rho(z, z', t|\beta) &= \Delta\,\exp\left\{i\frac{mt}{2\hbar}[z - z']\frac{[a(2 + t^2\omega^2) + \omega^2(z + z')]}{1 + \omega^2 t^2}\right\} \\ &\times \exp\left(-\frac{\pi}{2}\Delta^2\{[a^2t^4 - 2at^2(z + z') + 2(z^2 + z'^2)] \times \cosh(\beta\hbar\omega) - [at^2 - 2z][at^2 - 2z']\}\right),\end{aligned} \tag{25}$$

where

$$\Delta = \sqrt{\frac{m\omega}{2\pi\hbar(1 + \omega^2 t^2)\,\sinh(\beta\hbar\omega)}}. \tag{26}$$

The average position of the atomic cloud gives

$$\bar{z}(t) = \frac{\int z\rho(z, z, t|\beta)dz}{\int \rho(z, z, t|\beta)dz} = \frac{at^2}{2}, \tag{27}$$

which is the expected result for a free fall starting at rest [Eq. (7)]. The width of the atomic cloud is

$$\begin{aligned}\sigma_z(t) &= \sqrt{\overline{z^2} - \bar{z}^2} \\ &= \sqrt{\frac{\hbar(1 + t^2\omega^2)}{2m\omega}\coth(\theta)} \\ &\simeq \sqrt{\sigma_z^2(0) + (v_{\mathrm{rms}}t)^2},\end{aligned} \tag{28}$$

where in the last expression we considered the near-classical regime with $\sigma_z(0) = \sqrt{k_B T_0/m\omega^2}$. The axial expansion velocity is given by v_{rms} [60]. Note that $\sigma_z(0)$ equals the position at which the potential energy $(m\omega^2 x^2/2)$ matches the thermal energy $(k_B T_0/2)$. The term $\sqrt{\hbar/2m\omega}$ in Eq. (28) corresponds to the standard deviation in position of the ground-state wave function of the harmonic oscillator. Similarly, the width of the atomic cloud in momentum space is

$$\sigma_{p_z}(t) = \sqrt{\frac{m\hbar\omega}{2}\coth(\theta)} \simeq \sqrt{mk_B T_0} = mv_{\mathrm{rms}}, \tag{29}$$

and at $t = 0$ we have

$$\sigma_z^2(0)\sigma_{p_z}^2(0) = \frac{\hbar^2}{4}\coth^2(\theta), \tag{30}$$

which approaches a minimum uncertainty wave function in the quantum regime ($\theta \gg 1, T \to 0$).

Notice that the wave-packet expansion of Eq. (9) has a similar time dependence as Eq. (28) with $\hbar/2m\sigma_z(0)$ replaced by $v_{\rm rms}$. In both cases, the width remains constant at short times and has a linear growth at long times with a velocity determined by the uncertainty principle [Eq. (9)] or the temperature [Eq. (28)], respectively. To reach a high precision with the gravimeter, we are interested in long expansion times, so we can ignore the initial size. Then, the interrogation time before reaching the size Δz_r is limited to

$$t_2 = \frac{1}{v_{\rm rms}}\Delta z_r = 4T. \tag{31}$$

Here, we see that the measurement time (t_2) is proportional to $\sqrt{P/\eta^2 T_0}$. Taking a power of $P = 1$ W, a magnetic-field gradient of $\eta = 0.05$ Tm^{-1}, a temperature of 1 μK, an area of $A = 60$ cm^2, and $\xi = 0.2$ gives $t_2 = 2.3$ ms. This time is shorter than before, but it can still increase by changing the power and the gradient. The precision in the measurement of g gives

$$\frac{\sigma_g}{g} = \frac{\sigma_{\Delta\Phi}\zeta^2}{b_2 g\xi^3}\left(\frac{AT_0}{P}\right)^{3/2}, \tag{32}$$

with

$$b_2 = \frac{3\sqrt{6}\pi^3}{16}\left(\frac{\mu_0 m\langle e|\mu_z|g\rangle^2}{ck_B\hbar^2}\right)^{3/2}. \tag{33}$$

This regime gives a different dependence on the experimental parameters compared to Eq. (18).

We impose similar constraints as in the previous section. Having pulses smaller than the time between pulses [analogous to Eq. (20)] gives

$$P \gg \frac{c}{\sqrt{3}\mu_0}\left(\frac{\hbar}{\langle e|\mu_z|g\rangle}\right)^2\frac{A\zeta v_{\rm rms}}{\xi}. \tag{34}$$

Limiting the free fall to a maximum available distance $z_{\rm max}$ [analogous to Eq. (22)] gives

$$P \leqslant \frac{c}{3\pi^2\mu_0 g}\left(\frac{\hbar}{\langle e|\mu_z|g\rangle}\right)^2\frac{A\zeta^2 z_{\rm max}v_{\rm rms}^2}{\xi^2}. \tag{35}$$

The condition for the simultaneous application of the π pulses for the wave functions at each path with two different frequencies [analogous to Eq. (23)] gives

$$P \gg \left(\frac{512m^2c}{3\pi^2\mu_0\langle e|\mu_z|g\rangle^2}\right)\frac{Av_{\rm rms}^4}{\xi^2}. \tag{36}$$

Notice that this last expression is independent of the magnetic-field gradient. The reason for the nonintuitive direction of the inequality was already explained in Eq. (23).

Figure 3 shows the precision that can be obtained in a single measurement as a function of the experimental parameters, as well as the excluded regions from the conditions above. The dominant constraint is the one given by Eq. (36),

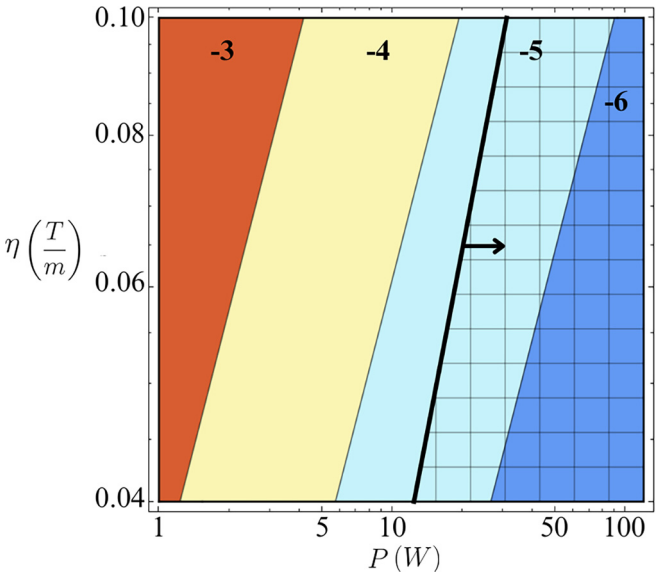

FIG. 3. Projected fractional precision of the measurement of g as a function of the microwave power (P) and magnetic-field gradient (η) for a sample initially trapped in thermal equilibrium. The color code corresponds to the number of significant digits attainable in a single measurement, determined by the computation of $\log_{10}(\sigma_g/g)$ using Eq. (32). We use $A = 60$ cm^2, $\sigma_{\Delta\Phi} = 0.003$, $\xi = 0.2$, $T_0 = 1$ μK, $z_{\rm max} = 50$ cm. We show the boundary set by Eq. (34) (black solid line). The limits defined by Eqs. (21) and (35) lie outside of the figure and they do not add any restrictions. For the case of two independent microwave sources, the limit imposed by Eq. (36) defines a more strict condition that cannot be fulfilled in the region shown. The mesh pattern indicates the region that fulfills all the conditions for the case of a single microwave source.

which corresponds to the simultaneous excitation of the π pulses with two different microwave sources. The boundary of this restriction excludes all the regions shown, thus the required microwave power might be prohibitively large and an alternative approach is needed.

Instead of implementing the π pulses with two different microwave sources as proposed from the condition of Eq. (12), we switch to applying the π pulse for the wave packets in both paths with a single microwave source. This is achieved while the resonant region [Δz_r, Eq. (5)] is larger than the separation distance between the center of the wave packets [$\Delta d(T)$, Eq. (11)], that is, $\Delta z_r \geqslant \Delta d(T)$. This results in an upper limit for the time between pulses of

$$T = \left[\frac{24\mu_0 m^2\langle e|\mu_z|g\rangle^2}{c\hbar^4\zeta^4}\left(\frac{\xi^2 P}{A}\right)\right]^{1/4}. \tag{37}$$

Taking a power of $P = 1$ W, a magnetic-field gradient of $\eta = 0.05$ Tm^{-1}, an area of $A = 60$ cm^2, and $\xi = 0.2$ gives a measurement time of $4T = 8$ ms. This time scales as $\sqrt[4]{P}/\eta$ and sets the precision in the measurement of g as follows:

$$\frac{\sigma_g}{g} = \frac{\sigma_{\Delta\Phi}\zeta^2}{b_3 g\xi^{3/2}}\left(\frac{A}{P}\right)^{3/4}, \tag{38}$$

where

$$b_3 = 2\left(\frac{24\mu_0 m^2 \langle e|\mu_z|g\rangle^2}{c\hbar^4}\right)^{3/4}. \tag{39}$$

To compute the precision in the measurement of g, for a given available power (P) and magnetic-field gradient (η), we take the minimum time (T) between Eqs. (31) and (37) (to be compatible with both restrictions), giving either Eq. (32) or Eq. (38) for the precision. For the parameter values shown in Fig. 3, the limiting time is given by Eq. (31), giving the same relative precision as described before [Eq. (32)]. The difference is that the restriction from Eq. (36) no longer applies and there is a region now that fulfills all the conditions, as indicated by the mesh pattern.

C. Discussion about the two regimes

The precision shown in Fig. 2 for the expansion from a pure state is much higher than that of Fig. 3 for a sample initially trapped at some temperature. Even when the first one shows the ultimate limitations of this gravimetric method, it considers atoms initially at rest, with zero temperature. We recover the contribution from the thermal motion in the second case, and therefore, this gives a more appropriate calculation of the precision limits at a finite temperature. Adopting a dipole trap increases the complexity of the experimental setup. We can consider instead having an atomic cloud in a magneto-optical trap (MOT) at the same temperature. Then, by adding an initial position selection pulse, we can choose a slice of the cloud of atoms in the MOT that would have a similar initial state as the one used for the dipole trap, at the price of reducing the number of atoms. The fractional precision that can be reached in a single measurement of g for the parameters considered in Fig. 3 approaches 10^{-7}. This is very reasonable and allows for a 1-μGal precision after an average time of about 1 h.

Figure 3 shows the parameter region (mesh pattern) that fulfills all the conditions we have introduced and allows therefore for an experimental demonstration. Out of those restrictions, the one given by Eq. (34) (black solid line in Fig. 3) is the most important one, which corresponds to having pulses with a duration much smaller than the time between them. Equation (34) establishes a minimum power that must be applied for this kind of measurement. The use of cavities might be helpful to reach the high microwave powers needed. In reality, it is a requirement on the minimum value for the Rabi frequency [$\Omega_0 > (32/\pi\sqrt{3})mv_{\rm rms}^2/\hbar\xi^2$], which in the case of the microwave excitation depends on the power (P) and the area (A). For example, an $A = 60$ cm^2 and a $P = 100$ W correspond to a minimum Rabi frequency of $\Omega_0 \simeq 10^5$ s^{-1}. If copropagating Raman transitions are used instead, it is still necessary to achieve that same Rabi frequency. This minimum power scales as $v_{\rm rms}^4 \propto T_0^2$. Therefore colder samples require a smaller microwave power. Including an evaporative cooling stage adds to the complexity of the gravimeter and might not be the most desirable option for a portable device. An alternative might be to measure the signal at the end of the sequence from just the atoms in the central slice of the atomic cloud which correspond to atoms with a smaller velocity spread, at the price of having a reduction in the number of atoms for the measurement.

Lastly, it is noteworthy that the visibility loss stemming from the quadratic Zeeman contribution [42], as well as from factors such as gravity gradients [56,57] and nonlinear terms in the gravitational potential [58], does not pose an issue within the scope of the timeframes we consider [constrained by Eq. (31)]. Nevertheless, if powers higher than 100 W are used (situated to the right of the depicted region in Fig. 3), the measurement time escalates to a point where the loss of visibility caused by the aforementioned effects becomes significant enough to warrant closer scrutiny.

IV. CONCLUSIONS

A magnetic T^3-atomic gravimeter is an attractive option for portable devices due to its simplicity because it eliminates the need for Raman beams. We analyzed the precision limits of this gravimeter due to the expansion of the atomic cloud. The thermal velocity spread of the cloud determines the maximum measurement time (and therefore the precision) that maintains resonant excitation over all the atoms. A higher microwave power or a lower magnetic-field gradient increases the size of the spatial region of resonant excitation. We analyzed the constraints that must be fulfilled to do the measurement leaving for future work the analysis of the systematic contributions. The dominant requirement is that there is a minimum power required to do the measurement, which is related to the condition of having excitation pulses with a duration smaller than the time between pulses. We found that the limits in the precision of the method due to the cloud expansion are still acceptable for many field applications, making this an attractive alternative for the design of portable devices.

ACKNOWLEDGMENT

We wish to acknowledge the financial support of the Mexican councils Consejo Potosino de Ciencia y Tecnologia (COPOCYT) Grant No. 23871 and Consejo Nacional de Ciencia y Tecnologia (CONACYT) Grant No. CF G40.

APPENDIX A: DENSITY MATRIX FOR AN ATOMIC SAMPLE TRAPPED IN THERMAL EQUILIBRIUM

The following calculation to compute the density matrix for a thermal ensemble in a harmonic potential follows the method described in Ref. [62]. Let us define the nonnormalized density matrix by

$$\rho_u \equiv e^{-\beta H}, \tag{A1}$$

with $\beta = 1/k_B T_0$. Taking the derivative with respect to β in the position representation gives

$$-\frac{\partial \rho_u(z, z'|\beta)}{\partial \beta} = H\rho_u(z, z'|\beta), \tag{A2}$$

with the condition that in the limit where $\beta \longrightarrow 0$ (or $T_0 \longrightarrow \infty$), we recover the density matrix of a completely random ensemble, i.e., $\rho_u(z, z'|0) = \delta(z - z')$. This differential equation is known as a Bloch differential equation [60,63].

We approximate the potential in an optical dipole trap of oscillating frequency ω with a harmonic oscillator [64]:

$$H = \frac{P_z^2}{2m} + \frac{m\omega^2 Z^2}{2}. \tag{A3}$$

Thus, Eq. (A2) becomes

$$-\frac{\partial \rho_u}{\partial \theta} = -\frac{\partial^2 \rho_u}{\partial \chi^2} + \chi^2 \rho_u, \tag{A4}$$

where we have introduced the nondimensional quantities

$$\chi \equiv \sqrt{\frac{m\omega}{\hbar}} z, \quad \theta \equiv \frac{\hbar\omega}{2}\beta, \tag{A5}$$

and the initial condition is given by $\rho(\chi, \chi'|0) = \sqrt{m\omega/\hbar}\,\delta(\chi - \chi')$. The solution is

$$\rho_u(\chi, \chi'|\beta) = \sqrt{\frac{m\omega}{2\pi\hbar\,\sinh(2\theta)}}\,\exp\left\{-\frac{\coth(2\theta)}{2} \times [\chi^2 - 2\chi'\chi\,\mathrm{sech}(2\theta) + \chi'^2]\right\}. \tag{A6}$$

The position distribution is given by the diagonal elements of the density matrix:

$$\rho_u(z, z|\beta) = \sqrt{\frac{m\omega}{2\pi\hbar\,\sinh(2\theta)}}\,\exp\left[-\frac{m\omega}{\hbar} z^2\,\tanh(\theta)\right]. \tag{A7}$$

This same result can be derived using alternative approaches [65,66]. In the near-classical regime, i.e., $\theta \ll 1$, Eq. (A6) becomes

$$\rho_u(z, z'|\beta) = \frac{1}{\Xi\sqrt{2\pi}}\,\exp\left[-\frac{(z-z')^2}{2\Xi^2}\right], \tag{A8}$$

where we have defined $\Xi^2 = \hbar^2/(2mkT_0)$. Note that

$$\lim_{\theta\to 0^+} \rho_u(z, z'|\beta) = \delta(z - z'), \tag{A9}$$

as required, and that Ξ is proportional to the thermal de Broglie wavelength $\Lambda = \sqrt{\frac{\hbar^2}{mkT_0}}$, which is inversely proportional to the partition function of a monoatomic gas and establishes the condition of applicability of the Boltzmann statistics when compared against the dimensions of the container [60].

APPENDIX B: FREE-FALL EVOLUTION OF THE DENSITY MATRIX

When atoms are trapped in an optical dipole trap and the trap is turned off instantaneously, we can assume that the state right after remains unchanged. Therefore, we use the initial state given by Eq. (A6). The free-fall Hamiltonian with acceleration a is

$$H = \frac{P_z^2}{2m} + maZ. \tag{B1}$$

We calculate the evolution of the density matrix in the momentum representation [67]

$$\langle p|\rho(t)|p'\rangle = \langle p|U^\dagger \rho(0) U|p'\rangle = \langle p(t)|\rho(0)|p'(t)\rangle, \tag{B2}$$

where $\rho(0)$ is the momentum representation of $\rho(\chi, \chi'|\beta)$ [Eq. (A6)], and

$$U = \exp\left[-\frac{i}{\hbar}\left(\frac{P_z^2}{2m} + maZ\right)t\right]. \tag{B3}$$

At first order (by ignoring quadratic terms in time) the time evolution operator can be factorized as $\exp(-\frac{i}{\hbar}\frac{P_z^2}{2m}t)\exp(-\frac{i}{\hbar}maZt)$. Thus, by recognizing the second exponential as the generator of translation in momentum space, the time evolution of the momentum eigenstate can be calculated using the split-operator method [68–71]. The result is

$$|p(t)\rangle = \exp\left[-\frac{i}{2\hbar m}\left(p^2 t - pmat^2 + \frac{m^2 a^2 t^3}{3}\right)\right] \times |p - mat\rangle. \tag{B4}$$

Inserting this into Eq. (B2) we get

$$\rho(p, p', t|\beta) = e^{-i\omega_{p,p'}t}\,\rho(p - mat, p' - mat, 0|\beta), \tag{B5}$$

where

$$\omega_{p,p'} = \frac{1}{2m\hbar}[(p^2 - p'^2) - (p - p')mat]. \tag{B6}$$

The density matrix in the momentum representation gives

$$\rho(p, p', t|\beta) = e^{-i\omega_{p,p'}t}\sqrt{\frac{\mathrm{csch}(\beta\hbar\omega)}{2\pi\hbar m\omega}} \times \exp\left(-\frac{\{[(p - mat)^2 + (p' - mat)^2]\,\coth(\beta\hbar\omega) - 2[p - mat][p' - mat]\,\mathrm{csch}(\beta\hbar\omega)\}}{2m\hbar\omega}\right), \tag{B7}$$

and the corresponding form in the position representation is

$$\rho(z, z', t|\beta) = \Delta\exp\left\{i\frac{mt}{2\hbar}[z - z']\frac{[a(2 + t^2\omega^2) + \omega^2(z + z')]}{1 + \omega^2 t^2}\right\} \times \exp\left(-\frac{\pi}{2}\Delta^2\{[a^2t^4 - 2at^2(z + z') + 2(z^2 + z'^2)]\,\cosh(\beta\hbar\omega) - [at^2 - 2z][at^2 - 2z']\}\right), \tag{B8}$$

with Δ defined in Eq. (26). The position distribution obtained from the diagonal elements is

$$\rho(z, z, t|\beta) = \Delta\exp\left\{-\frac{\pi}{2}\Delta^2[(a^2t^4 - 4at^2 z + 4z^2)\,\cosh(\beta\hbar\omega) - (at^2 - 2z)^2]\right\}. \tag{B9}$$

[1] S. Abend, M. Gersemann, C. Schubert, D. Schlippert, E. M. Rasel, M. Zimmermann, M. A. Efremov, A. Roura, F. A. Narducci, and W. P. Schleich, Atom interferometry and its applications, arXiv:2001.10976.

[2] J. M. Hogan, D. M. S. Johnson, and M. A. Kasevich, Light-pulse atom interferometry, arXiv:0806.3261.

[3] T. L. Gustavson, P. Bouyer, and M. A. Kasevich, Precision rotation measurements with an atom interferometer gyroscope, Phys. Rev. Lett. **78**, 2046 (1997).

[4] T. L. Gustavson, A. Landragin, and M. A. Kasevich, Rotation sensing with a dual atom-interferometer Sagnac gyroscope, Class. Quantum Grav. **17**, 2385 (2000).

[5] M. J. Snadden, J. M. McGuirk, P. Bouyer, K. G. Haritos, and M. A. Kasevich, Measurement of the Earth's gravity gradient with an atom interferometer-based gravity gradiometer, Phys. Rev. Lett. **81**, 971 (1998).

[6] A. Peters, K. Y. Chung, and S. Chu, High-precision gravity measurements using atom interferometry, Metrologia **38**, 25 (2001).

[7] N. Robins, P. Altin, J. Debs, and J. Close, Atom lasers: Production, properties and prospects for precision inertial measurement, Phys. Rep. **529**, 265 (2013).

[8] S. Dimopoulos, P. W. Graham, J. M. Hogan, M. A. Kasevich, and S. Rajendran, Atomic gravitational wave interferometric sensor, Phys. Rev. D **78**, 122002 (2008).

[9] S. Dimopoulos, P. W. Graham, J. M. Hogan, M. A. Kasevich, and S. Rajendran, Gravitational wave detection with atom interferometry, Phys. Lett. B **678**, 37 (2009).

[10] J. Harms, B. J. J. Slagmolen, R. X. Adhikari, M. C. Miller, M. Evans, Y. Chen, H. Müller, and M. Ando, Low-frequency terrestrial gravitational-wave detectors, Phys. Rev. D **88**, 122003 (2013).

[11] R. Bouchendira, P. Cladé, S. Guellati-Khélifa, F. Nez, and F. Biraben, New determination of the fine structure constant and test of the quantum electrodynamics, Phys. Rev. Lett. **106**, 080801 (2011).

[12] J. B. Fixler, G. T. Foster, J. M. McGuirk, and M. A. Kasevich, Atom interferometer measurement of the Newtonian constant of gravity, Science **315**, 74 (2007).

[13] H. Müller, S.-W. Chiow, S. Herrmann, S. Chu, and K.-Y. Chung, Atom-interferometry tests of the isotropy of post-Newtonian gravity, Phys. Rev. Lett. **100**, 031101 (2008).

[14] V. Ménoret, P. Vermeulen, N. Le Moigne, S. Bonvalot, P. Bouyer, A. Landragin, and B. Desruelle, Gravity measurements below 10^{-9} g with a transportable absolute quantum gravimeter, Sci. Rep. **8**, 12300 (2018).

[15] B. Stray, A. Lamb, A. Kaushik, J. Vovrosh, A. Rodgers, J. Winch, F. Hayati, D. Boddice, A. Stabrawa, A. Niggebaum, M. Langlois, Y.-H. Lien, S. Lellouch, S. Roshanmanesh, K. Ridley, G. de Villiers, G. Brown, T. Cross, G. Tuckwell, A. Faramarzi, N. Metje, K. Bongs, and M. Holynski, Quantum sensing for gravity cartography, Nature (London) **602**, 590 (2022).

[16] B. Chen, J. Long, H. Xie, C. Li, L. Chen, B. Jiang, and S. Chen, Portable atomic gravimeter operating in noisy urban environments, Chin. Opt. Lett. **18**, 090201 (2020).

[17] M. Van Camp, O. de Viron, A. Watlet, B. Meurers, O. Francis, and C. Caudron, Geophysics from terrestrial time-variable gravity measurements, Rev. Geophys. **55**, 938 (2017).

[18] W. Torge and J. Müller, *Geodesy* (De Gruyter, Berlin, 2012).

[19] J. Padín, A. Martín, and A. B. Anquela, Archaeological microgravimetric prospection inside don church (Valencia, Spain), J. Archaeol. Sci. **39**, 547 (2012).

[20] J. Panisova, M. Fraštia, T. Wunderlich, R. Pašteka, and D. Kušnirák, Microgravity and ground-penetrating radar investigations of subsurface features at the St Catherine's Monastery, Slovakia, Archaeol. Prospect. **20**, 163 (2013).

[21] I. Bishop, P. Styles, S. J. Emsley, and N. S. Ferguson, The detection of cavities using the microgravity technique: Case histories from mining and karstic environments, Geol. Soc. London Eng. Geol. Special Pub. **12**, 153 (1997).

[22] D. Carbone, M. P. Poland, M. Diament, and F. Greco, The added value of time-variable microgravimetry to the understanding of how volcanoes work, Earth-Science Rev. **169**, 146 (2017).

[23] A. D. Cronin, J. Schmiedmayer, and D. E. Pritchard, Optics and interferometry with atoms and molecules, Rev. Mod. Phys. **81**, 1051 (2009).

[24] F. A. Narducci, A. T. Black, and J. H. Burke, Advances toward fieldable atom interferometers, Adv. Phys.: X **7**, 1946426 (2022).

[25] J. E. Debs, K. S. Hardman, P. A. Altin, G. McDonald, J. D. Close, and N. P. Robins, From apples to atoms: Measuring gravity with ultra cold atomic test masses, Preview **2013**, 30 (2013).

[26] M. Kasevich and S. Chu, Atomic interferometry using stimulated Raman transitions, Phys. Rev. Lett. **67**, 181 (1991).

[27] M. Kasevich and S. Chu, Measurement of the gravitational acceleration of an atom with a light-pulse atom interferometer, Appl. Phys. B **54**, 321 (1992).

[28] M. Weitz, T. Heupel, and T. W. Hänsch, Multiple beam atomic interferometer, Phys. Rev. Lett. **77**, 2356 (1996).

[29] P. D. Featonby, G. S. Summy, C. L. Webb, R. M. Godun, M. K. Oberthaler, A. C. Wilson, C. J. Foot, and K. Burnett, Separated-path Ramsey atom interferometer, Phys. Rev. Lett. **81**, 495 (1998).

[30] J. M. McGuirk, M. J. Snadden, and M. A. Kasevich, Large area light-pulse atom interferometry, Phys. Rev. Lett. **85**, 4498 (2000).

[31] H. Müller, S.-W. Chiow, Q. Long, S. Herrmann, and S. Chu, Atom interferometry with up to 24-photon-momentum-transfer beam splitters, Phys. Rev. Lett. **100**, 180405 (2008).

[32] P. Cladé, S. Guellati-Khélifa, F. Nez, and F. Biraben, Large momentum beam splitter using Bloch oscillations, Phys. Rev. Lett. **102**, 240402 (2009).

[33] G. D. McDonald, C. C. N. Kuhn, S. Bennetts, J. E. Debs, K. S. Hardman, M. Johnsson, J. D. Close, and N. P. Robins, $80\hbar k$ momentum separation with Bloch oscillations in an optically guided atom interferometer, Phys. Rev. A **88**, 053620 (2013).

[34] K. Kotru, D. L. Butts, J. M. Kinast, and R. E. Stoner, Large-area atom interferometry with frequency-swept Raman adiabatic passage, Phys. Rev. Lett. **115**, 103001 (2015).

[35] S.-W. Chiow, T. Kovachy, H.-C. Chien, and M. A. Kasevich, $102\hbar k$ large area atom interferometers, Phys. Rev. Lett. **107**, 130403 (2011).

[36] B. Plotkin-Swing, D. Gochnauer, K. E. McAlpine, E. S. Cooper, A. O. Jamison, and S. Gupta, Three-path atom interferometry

with large momentum separation, Phys. Rev. Lett. **121**, 133201 (2018).
[37] J. Rudolph, T. Wilkason, M. Nantel, H. Swan, C. M. Holland, Y. Jiang, B. E. Garber, S. P. Carman, and J. M. Hogan, Large momentum transfer clock atom interferometry on the 689 nm intercombination line of strontium, Phys. Rev. Lett. **124**, 083604 (2020).
[38] M. Gebbe, J.-N. Siemß, M. Gersemann, H. Müntinga, S. Herrmann, C. Lämmerzahl, H. Ahlers, N. Gaaloul, C. Schubert, K. Hammerer, S. Abend, and E. M. Rasel, Twin-lattice atom interferometry, Nat. Commun. **12**, 2544 (2021).
[39] M. Zimmermann, M. A. Efremov, W. Zeller, W. P. Schleich, J. P. Davis, and F. A. Narducci, Representation-free description of atom interferometers in time-dependent linear potentials, New J. Phys. **21**, 073031 (2019).
[40] G. D. McDonald, C. C. N. Kuhn, S. Bennetts, J. E. Debs, K. S. Hardman, J. D. Close, and N. P. Robins, A faster scaling in acceleration-sensitive atom interferometers, Europhys. Lett. **105**, 63001 (2014).
[41] G. D. McDonald and C. C. N. Kuhn, Space-time area in atom interferometry, arXiv:1312.2713.
[42] D. Comparat, Limitations for field-enhanced atom interferometry, Phys. Rev. A **101**, 023606 (2020).
[43] M. Zimmermann, M. A. Efremov, A. Roura, W. P. Schleich, S. A. DeSavage, J. P. Davis, A. Srinivasan, F. A. Narducci, S. A. Werner, and E. M. Rasel, T^3-interferometer for atoms, Appl. Phys. B **123**, 102 (2017).
[44] J. E. Palmer and S. D. Hogan, Electric Rydberg-atom interferometry, Phys. Rev. Lett. **122**, 250404 (2019).
[45] B.-G. Englert, J. Schwinger, and M. O. Scully, Is spin coherence like Humpty-Dumpty? I. Simplified treatment, Found. Phys. **18**, 1045 (1988).
[46] J. Schwinger, M. O. Scully, and B.-G. Englert, Is spin coherence like Humpty-Dumpty? Z. Phys. D **10**, 135 (1988).
[47] M. O. Scully, B.-G. Englert, and J. Schwinger, Spin coherence and Humpty-Dumpty. III. The effects of observation, Phys. Rev. A **40**, 1775 (1989).
[48] O. Amit, Y. Margalit, O. Dobkowski, Z. Zhou, Y. Japha, M. Zimmermann, M. A. Efremov, F. A. Narducci, E. M. Rasel, W. P. Schleich, and R. Folman, T^3 Stern-Gerlach matter-wave interferometer, Phys. Rev. Lett. **123**, 083601 (2019).
[49] Y. Margalit, O. Dobkowski, Z. Zhou, O. Amit, Y. Japha, S. Moukouri, D. Rohrlich, A. Mazumdar, S. Bose, C. Henkel, and R. Folman, Realization of a complete Stern-Gerlach interferometer: Toward a test of quantum gravity, Sci. Adv. **7**, eabg2879 (2021).
[50] C. Oh, H. Kwon, L. Jiang, and M. S. Kim, Field-gradient measurement using a Stern-Gerlach atomic interferometer with butterfly geometry, Phys. Rev. A **102**, 053321 (2020).
[51] Y. Japha and R. Folman, Quantum uncertainty limit for Stern-Gerlach interferometry with massive objects, Phys. Rev. Lett. **130**, 113602 (2023).
[52] R. Karcher, A. Imanaliev, S. Merlet, and F. P. D. Santos, Improving the accuracy of atom interferometers with ultracold sources, New J. Phys. **20**, 113041 (2018).
[53] P. Wolf and P. Tourrenc, Gravimetry using atom interferometers: Some systematic effects, Phys. Lett. A **251**, 241 (1999).
[54] L. O. Castaños and E. Gomez, Model for a phase-space selector using microwave transitions, Phys. Rev. A **89**, 013406 (2014).
[55] It remains to quantify the systematic shift onto the gravimetric measurement due to $\delta(z)$.
[56] D. N. Aguilera, H. Ahlers, B. Battelier, A. Bawamia, A. Bertoldi, R. Bondarescu, K. Bongs, P. Bouyer, C. Braxmaier, L. Cacciapuoti *et al.*, Ste-quest: Test of the universality of free fall using cold atom interferometry, Class. Quantum Grav. **31**, 115010 (2014).
[57] A. Roura, W. Zeller, and W. P. Schleich, Overcoming loss of contrast in atom interferometry due to gravity gradients, New J. Phys. **16**, 123012 (2014).
[58] A. Bertoldi, F. Minardi, and M. Prevedelli, Phase shift in atom interferometers: Corrections for nonquadratic potentials and finite-duration laser pulses, Phys. Rev. A **99**, 033619 (2019).
[59] S. Dimopoulos, P. W. Graham, J. M. Hogan, and M. A. Kasevich, General relativistic effects in atom interferometry, Phys. Rev. D **78**, 042003 (2008).
[60] D. A. McQuarrie, *Statistical Mechanics*, Harper's Chemistry Series (Longman, London, 1976).
[61] F. Reif, *Berkeley Physics Course: Statistical Physics Vol. 5* (McGraw-Hill, New York, 1967), Chap. 6, pp. 224–226.
[62] R. P. Feynman, *Statistical Mechanics: A Set of Lectures*, 7th ed. (Perseus, Boulder, CO, 1972), Chap. 2, pp. 46–53.
[63] N. March and L. Nieto, Bloch equation for the canonical density matrix in terms of its diagonal element: The slater sum, Phys. Lett. A **373**, 1691 (2009).
[64] H. J. Metcalf and P. van der Straten, Optical traps for neutral atoms, in *Laser Cooling and Trapping* (Springer, New York, 1999), pp. 149–164.
[65] S. Ghonge and D. C. Vural, Temperature as a quantum observable, J. Stat. Mech.: Theory Exp. (2018) 073102.
[66] L. F. Barragán-Gil and R. Walser, Harmonic oscillator thermal density matrix: First-order differential equations for the position representation, Am. J. Phys. **86**, 22 (2018).
[67] From now on, we simply write ρ instead of ρ_u for the solution of Eq. (A2).
[68] M. Feit, J. Fleck, and A. Steiger, Solution of the Schrödinger equation by a spectral method, J. Comput. Phys. **47**, 412 (1982).
[69] C. Leforestier, R. Bisseling, C. Cerjan, M. Feit, R. Friesner, A. Guldberg, A. Hammerich, G. Jolicard, W. Karrlein, H.-D. Meyer, N. Lipkin, O. Roncero, and R. Kosloff, A comparison of different propagation schemes for the time dependent Schrödinger equation, J. Comput. Phys. **94**, 59 (1991).
[70] P. Maksym and H. Aoki, Fast split operator method for computation of time dependent quantum states of bilayer graphene in a magnetic field, Physica E **112**, 66 (2019).
[71] S. MacNamara and G. Strang, Operator splitting, in *Splitting Methods in Communication, Imaging, Science, and Engineering*, edited by R. Glowinski, S. J. Osher, and W. Yin (Springer, New York, 2016), pp. 95–114.